Early detection of citrus anthracnose caused by Colletotrichum gloeosporioides using hyperspecral imaging.

TANG, Y., YANG, J., ZHUANG, J., HOU, C., MIAO, A., REN, J., HUANG, H., TAN, Z. and PALIWAL, J.

2023

Early detection of citrus anthracnose caused by *Colletotrichum gloeosporioides* using hyperspectral imaging

Yu Tang [a], Jiepeng Yang [a,1], Jiajun Zhuang [b,*], Chaojun Hou [b], Aimin Miao [b], Jinchang Ren [c], Huasheng Huang [a], Zhiping Tan [a], Jitendra Paliwal [d]

[a] *Academy of Interdisciplinary Studies, Guangdong Polytechnic Normal University, Guangzhou 510665, China*
[b] *Academy of Contemporary Agriculture Engineering Innovations, Zhongkai University of Agriculture and Engineering, Guangzhou 510225, China*
[c] *National Subsea Centre, Robert Gordon University, Aberdeen AB21 OBH, UK*
[d] *Department of Biosystems Engineering, University of Manitoba, E2-376, EITC, 75A Chancellor's Circle, Winnipeg R3T 2N2, Manitoba, Canada*

* Corresponding author. *E-mail address:* zhuangjiajun@zhku.edu.cn (J. Zhuang).

[1] The first two authors contributed equally to this manuscript and should be considered co-first authors.

A B S T R A C T

Citrus fruit are susceptible to *Colletotrichum gloeosporioides* infestation during postharvest and shelf storage. Early and accurate detection of citrus anthracnose is conducive for carrying out targeted pesticide control and mitigating the potential spread of the disease. An early citrus anthracnose detection method using hyperspectral imaging and machine learning techniques is proposed. The hyperspectral data of sound citrus fruits were first collected and served as healthy samples, which were then inoculated with *C. gloeosporioides* and were further divided into asymptomatic and symptomatic samples. To characterize the global and local grayscale differences of the susceptible samples in different band images, the mean spectrum of the region of interest (ROI) of each band image was extracted as the global spectral features; moreover, the ROI in each band was segmented into disjointed local regions using the contrast limited adaptive histogram equalization and the Otsu thresholding algorithm, where the mean spectrum of the local regions were extracted as the local spectral features, respectively. The global and local spectral features were then concatenated into fused spectral features. Finally, the performance of the fused features was evaluated using support vector machine (SVM), k-NN and random forest (RF). The results showed that, compared with the conventional spectral feature-based methods, the proposed fused spectral features combined with SVM obtained the optimal results, where the average detection accuracy reached 91.97%. Furthermore, after applying feature selection using the successive projections algorithm (SPA), the resultant dimensionally-reduced fused spectral features also obtained acceptable results, with an average detection accuracy of 91.04%.

Keywords:
Citrus anthracnose; Early detection; Hyperspectral imaging; Fused spectral features; Machine learning

1. Introduction

The flavour and nutrition of citrus fruit have made them popular a mong consumers and growers worldwide. However, citrus is susceptible to fungal diseases such as cyanobacteria, green mould and brown rot in postharvest transport and storage processes. The anthracnose caused by *Colletotrichum gloeosporioides* shows potential high infectiousness, where the delayed onset of rot symptoms caused by such fungal disease is often devastating and can lead to significant postharvest losses due to their rapid mitigation of large-scale spread (Zhang & Timmer, 2007). Therefore, early and accurate detection of *Colletotrichum gloeosporioides* in citrus fruit during the post-harvest and shelf storage stage, especially in the asymptomatic phase, is beneficial and crucial for both formulating targeted pesticide control strategy and avoiding mitigation of further spread of the disease.

The analysis of disease and symptom severity is extremely important for solving fundamental problems in plant stress biology, and traditionally, for crop-specific disease detection, direct detection of plant pathogens has been an effective means. Among serological and nucleic acid-based molecular detection methods, the enzyme-linked immunosorbent assay (ELISA) and polymerase chain reaction (PCR) have been widely used (Martinelli et al., 2015); these techniques can not only accurately detect diseases with visible spots but also enable early detection when symptoms are not visible, for the potential of ELISA and PCR application for early disease diagnosis (Ruiz-Ruiz et al., 2009;Tian et al., 2020). Although molecular techniques are sensitive, accurate and effective for symptomatic disease detection, they require tedious, specialized sampling procedures and can only be used on a limited number of plants (Saccon et al., 2017;Singh et al., 2020). In recent years, related research sought to achieve non-destructive detection of fruit diseases with the help of advanced imaging and computer techniques, and many advanced imaging techniques have been applied in crop disease detection, such as nuclear magnetic resonance imaging, photoacoustic imaging, and thermal imaging. In particular, hyperspectral imaging (HSI) techniques have been widely used in the detection of different plants and diseases through the fusion of spectra and images (Babellahi et al., 2020; Ma et al., 2023; Nadimi et al., 2021; Li et al., 2023). Zhang et al. used the second principal component image in principal component analysis and the (680/715) band ratio image, combined with a simple threshold method to detect the stem tips of four diseases of citrus, and the classification accuracy of healthy and defective citrus reached 96.63 % (Zhang et al., 2020). Lu et al. used hyperspectral images to identify two similar diseases, including tea white star disease and anthracnose, and achieved 95.77 % classification accuracy using an extreme learning machine model (Lu et al., 2021). In addition to the accurate detection of visible diseases, some studies also focus on the evaluation of different severities of diseases. For example, Jiang et al. used the successive projections algorithm and random forest (RF) model to detect the severity of different diseases and pests in mangrove leaves (Jiang et al., 2021). Gui et al. graded the detection of soybean mosaic disease with different infection degrees (Gui et al., 2021). Although these studies could realize disease detection in the symptomatic stage, asymptomatic stage disease detection remains a practical challenge.

For hyperspectral detection of crop diseases at the asymptomatic stage, some research has focused on finding the spectral wavelengths that characterize certain disease specificities in fruit or leaves. For example, Gao et al. identified six significant wavelengths using the least absolute shrinkage and selection operators and used least squares support vector machines for the early detection of grape leaf curl disease with

classification accuracy between 66.67 % and 89.93 % (Gao et al., 2020). Yeh et al. determined a set of spectral bands for differentiating healthy and asymptomatic leaves by partial least squares regression to study the development of strawberry leaf anthracnose and obtained a classification accuracy of 88 % by stepwise discriminant analysis (Yeh et al., 2016). Ardila et al. performed early detection of anthracnose-infected mangoes and achieved an average classification accuracy of 91 % in 29 bands identified by linear discriminant analysis for anthracnose in the asymptomatic stage (Ardila et al., 2020). While these studies identified specific bands for early detection, they are still only early studies based on spectral features; Some additional research has focused on more specific feature extraction, such as Weng extraction of spectral and texture features of the best wavelengths and principal component images. The least squares support vector machine classifier is used to classify healthy, infected (asymptomatic and symptomatic) and nutrient-deficient leaves, and the classification accuracy is over 90 % for the different test set samples (Weng et al., 2018). Similarly, in the latest study, Xuan et al. extracted not only the spectral features of the region of interest (ROI) but also the texture features of the first three principal component images using a greyscale co-occurrence matrix. A partial least squares discriminant analysis model was then developed to evaluate the effective wavelengths, texture features and their fusion for early detection of the disease. The results showed that the best performance was obtained using the fused dataset with a classification accuracy of 91.4 % compared to the models using spectral or texture features alone (Xuan et al., 2022). Most of the current work mainly focused on extracting global spectral features from the entire crop image or some selected ROI. It is worth noting that global descriptors are less sensitive to local variation than local descriptors (Sajadi & Fathi, 2020), and thus in such case, the spectral differences due to the changes in the physicochemical properties of localised regions in early disease detection might be omitted. Therefore, the combination of global and local features can provide a high degree of discriminatory and complementary information, which may further improve the detection accuracy of the crop diseases.

Although much work has focused on the detection of crop diseases using spectral imaging techniques, these studies mainly focused on spectral feature extraction from only the entire crop or the ROI of the hyperspectral data, while the description of the local information of the ROI was not considered. The presented work was aimed to extract complementary spectral information of citrus fruit infected by *C. gloeosporioides* from both global and local modalities. The main contributions were as follows: (1) under different bands, the local regions were adaptively segmented from the entire ROI using a combination of contrast limited adaptive histogram equalization (CLAHE) and the Otsu thresholding algorithm, (2) feature-level fusion was conducted by concatenating the extracted mean spectrum information from the entire ROI and local regions, and (3) the detection performance of citrus anthracnose was evaluated using different machine learning models.

2. Materials and methods

In this paper, combination of the global and local hyperspectral features is proposed to realize the early detection of citrus anthracnose. A shown in Fig. 1, the main process includes (1) spectral data acquisition, (2) spectral feature extraction, and (3) classification performance evaluation.

2.1. Sample preparation and data collection

1) Samples.

The test citrus fruit were the South African mandarin, of the Nadorcott variety, and a total of 40 sound fruits with similar maturity and size were prepared. The fruit were washed with 2 % (v/v) sodium hypochlorite solution for 3 min, rinsed with tap water, air-dried, and stored at 6 °C and 80 % relative humidity in a constant temperature and humidity incubator before use.

The test anthracnose fungus was *C. gloeosporioides*, provided by the Institute of Biotechnology, Zhejiang University, which was pathogenically isolated from naturally infected citrus anthracnose fruit and transplanted onto potato dextrose agar (PDA) medium, followed by the preparation of a suspension at a concentration of approximately 1×10^6 CFU/ml with the aid of a haemocytometer plate for subsequent fungal inoculation experiments.

2) Hyperspectral imaging system.

Fig. 2 shows the HSI system (GaiaField-V10E, Jiangsu Dualix Spectral Imaging Technology Co., Ltd, Wuxi, Jiangsu, China) used to collect the citrus spectral data, which included a hyperspectral camera and a data acquisition box. The camera model was GaiaFieldPro-V10E with a spectral range of 388–1025 nm, a spatial range of 960 × 1040 pixels and a spectral channel number of 360. The data acquisition box consisted of four 50 W halogen lamps (spectral range of 350–2500 nm) and an adjustable loading platform. In this experiment, the surface of the citrus was approximately 68 cm from the camera lens during the acquisition, and the acquisition parameters of the optimal imaging effect were obtained by adjusting the exposure time and focal length, in which the forward speed of the motor was 0.46 mm/s and the exposure time was 10.8 ms.

3) Hyperspectral data collection.

The spherical shape of citrus fruit leads to inhomogeneity of reflected light from the fruit skin in hyperspectral images (Jiang et al., 2016). To minimize this optical aberration, the central equatorial region of fruit was selected as the sampling points (Castorena et al., 2015). The hyperspectral samples of the 40 sound fruits were collected at 5 sampling points, resulting a total of 200 healthy (H) samples (Fig. 3A). The fruit were then scrubbed with 75 % alcohol, rinsed with distilled water and left to air dry.

The 40 citrus fruits were divided into an experimental group containing 30 fruits and a control group containing 10 fruits. The equatorial parts of these fruits were selected to construct sampling points at 120° intervals and marked with a marker pen in a circle with a radius of 5 cm, and then 20 μL *C. gloeosporioides* spore suspension was inoculated into the sampling points of the experimental group, while the control group was inoculated with sterile water. The hyperspectral samples for each sampling point of the experimental and control groups were captured every 12 h (h) after inoculation, lasting eight days (d) and the fruit were stored in an environment of 26 °C and 60 % relative humidity after collection.

For the control group, the collected data were served as the control (C) samples. For the experimental group, firstly, the collected hyperspectral data from the citrus before fungal infestation was served as the healthy (H) samples (Fig. 3A); secondly, for the citrus after fungal

infestation, the whole fungal infestation process was divided into two main stages, i.e., the anthracnose asymptomatic stage and symptomatic stage, in terms of the existence of any obvious difference of the citrus epidermis in the experimental group and that in the control group by experienced experts, where the collected hyperspectral data from the citrus involved in the anthracnose asymptomatic stage and symptomatic stage were served as the asymptomatic (A) samples (Fig. 3C) and symptomatic (S) samples (Fig. 3B), respectively. For the entire samples collection process, excluding sampling points for inoculation failure, resulting in a total of 1682 hyperspectral samples, including 632 healthy samples (200H + 432C), 522 asymptomatic samples and 528 symptomatic samples. The samples obtained were then divided into training, validation and test sets according to the principle of stratified folds, with the three data sets accounting for 6:2:2 respectively.

The development of the fungus within 2–8 d is shown in Fig. 4, in which the abscissa indicates the incubation time after inoculation, and the ordinate indicates the overall proportion of asymptomatic and symptomatic samples with anthracnose. It can be observed that symptomatic samples appeared on the 4th day after inoculation, and 4 d and 5 d were the fastest development period of anthracnose, with approximately half of the samples showing spots. On the 8th day, all samples showed symptoms.

To eliminate the effect of dark currents and inhomogeneous illumination on the image, the acquired hyperspectral data were calibrated using the minmax normalization formula, and the obtained relative reflectance hyperspectral data can be written as follows:

$$R_C = \frac{S_C - D_C}{W_c - D_C} \tag{1}$$

where S_C represents the sample raw DN value data, D_C represents the data collected against a dark background, and W_C represents the data collected from a 99 % reflectance whiteboard.

2.2. Spectral feature extraction

To reduce the impact of the reflex effect distributed on the citrus surface (Fig. 3) caused by the halogen lamps, and encouraged by the experimental setup as reported by Gao et al. (2020), the ROI was extracted from the hyperspectral data with the approximate the circled area with a radius about 10 pixels. Subsequently, the hyperspectral data of the ROI were decomposed from the perspective of the spectral dimension, and the band images of the ROI under 360 bands were obtained, as shown in Fig. 5. The first column in Fig. 6 shows the band images of ROI of different samples under the same band. It can be observed that there is a difference in the overall grey level of different samples, which allows for the detection of idiosyncratic samples using the mean spectrum. Moreover, regions with higher grey intensities (high greyscale regions) and regions with lower grey intensities (low greyscale regions) can be observed in the band images of ROI. The generation of this difference indicates that the objects under the pixel have different abilities to absorb light in that band with different intensities, which may be related to the change of the physicalized nature of the measured under that pixel, or it may be due to the ellipsoidal shape of the citrus fruit that causes the inhomogeneity of the reflected light in the hyperspectral data. In the early detection of crop diseases, small greyscale differences in the 360 band images may occur due to the development of the fungus, and these small local variations might be difficult to capture by using only global feature descriptors, which may pose further chal-lenges for early and accurate disease detection.

To express this differential feature information of the samples, as shown in Fig. 5, for different band images, in addition to extracting the conventional mean spectrum of the entire ROI (called global spectral features in this study and denoted as GSFs), a combination of the CLAHE and Otsu image thresholding algorithms was used to further segment the ROI into high and low greyscale regions adaptively. The histogram equalization could enhance the contrast of the spectral channel images. As shown in Fig. 6, little difference within the original image samples from the three categories could be found. Still, the resultant image samples show obvious local grey-level intensity distributions after processed by the CLAHE algorithm, which provides more detailed spectral information by re-allocating the grey-level intensity within each channel image. As shown in Fig. 6, CLAHE was first used to enhance the contrast of the band images to make the high greyscale regions with higher brightness and low greyscale regions with lower brightness in the original image more prominent, and then the Otsu image thresholding algorithm was applied to the processed band images to determine the image binarization segmentation threshold. The binary mask was matched with the original band images to segment the original image of high greyscale and low greyscale regions. The mean spectrum of the two local regions under different bands was subsequently extracted as the local spectral features of the high and low greyscale regions (denoted HSFs and LSFs in this study, respectively). Finally, the global and local spectral features were concatenated to form the fused spectral features characterizing different susceptible samples. The high and low greyscale regions generated by the CLAHE and OTSU processing were characterised in the original image, and the results are shown in the fourth and fifth columns of Fig. 6, from which it can be seen that the two local regions contain pixels with similar greyscale, respectively. The LSFs and HSFs extracted from these two regions can reflect the local greyscale differences in the band images of different samples. Different spectral features and their fusions were subsequently input into machine learning models to evaluate their classification effects.

2.3. Optimal wavelengths selection

The large amount of redundancy and collinearity in hyperspectral data can be detrimental to the computational complexity and robustness of the model, and the excessive number of spectral wavelengths is detrimental to practical industrial applications as well. Successive projections algorithm (SPA) is an effective hyperspectral feature selection algorithm that could well handle the multicollinearity involved in the spectrum and form an informative low-dimensional hyperspectral feature subset with lower computational complexity (Liu et al., 2014). Therefore, the SPA was adopted to select the minimum redundant variables for the high-dimensional hyperspectral data. The SPA first randomly selects data under one candidate variable to form the initial vector, identifies the next candidate variable with the next candidate variable with the largest projection value by comparing the size of the projection on the orthogonal subspace with vectors of other candidate variables, then introduces another candidate variable in each iteration through the same projection procedure to form a subset of candidate variables, and finally evaluates the subset of candidate variables using the root mean square error (RMSE) of the multiple linear regression (MLR) model to remove redundant wavelengths.

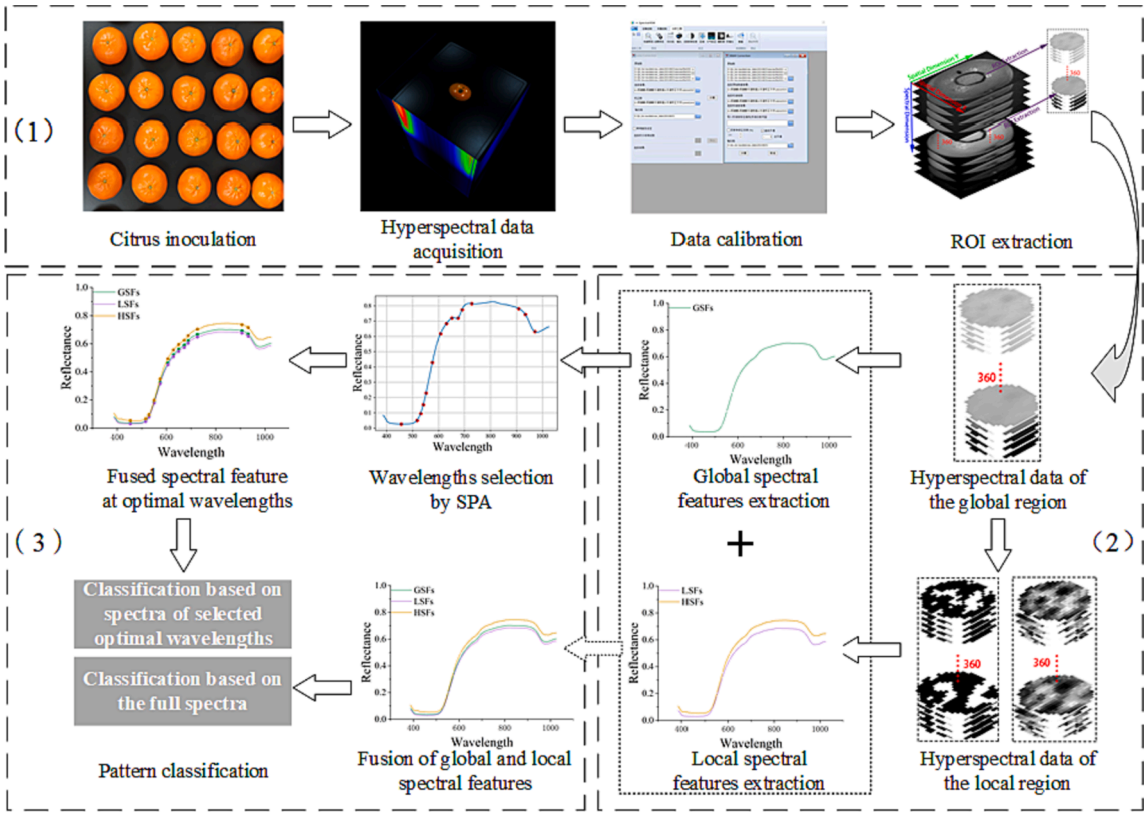

Fig. 1. Overview of the procedure schematic for early detection of citrus anthracnose.

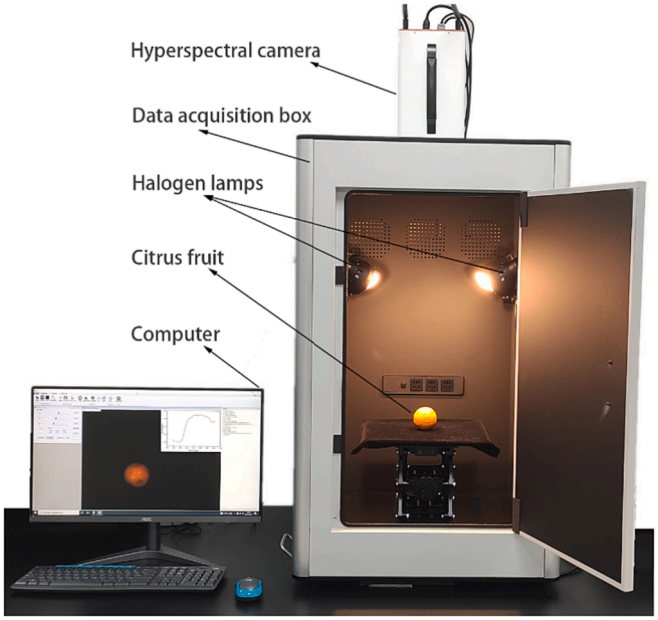

Fig. 2. Hyperspectral imaging system.

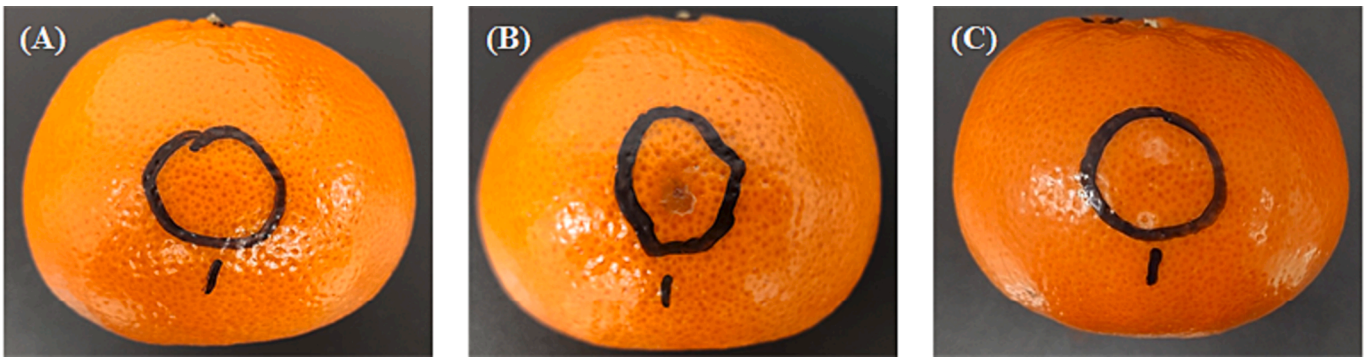

Fig. 3. Experimental citrus fruit with different levels of infection: (A) healthy, (B) symptomatic, (C) asymptomatic.

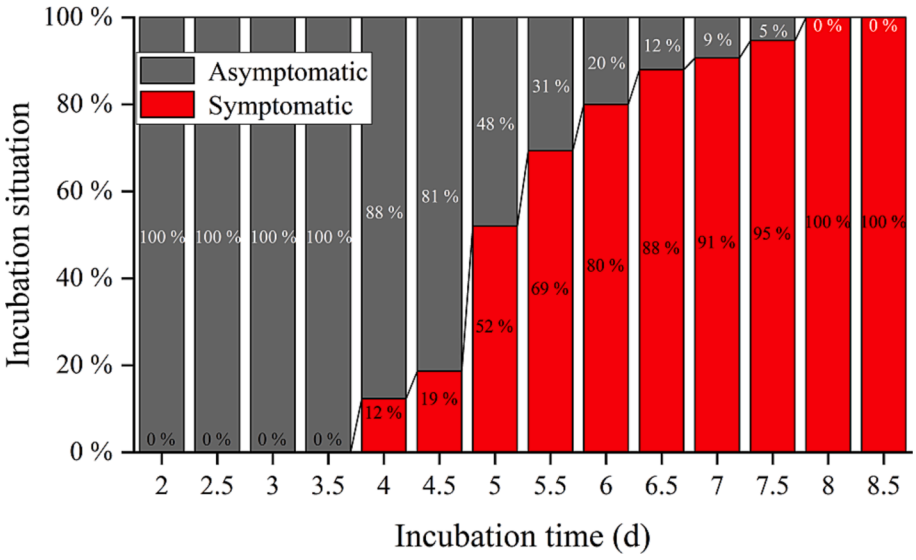

Fig. 4. Fungal development at inoculation sites within 2–8 d.

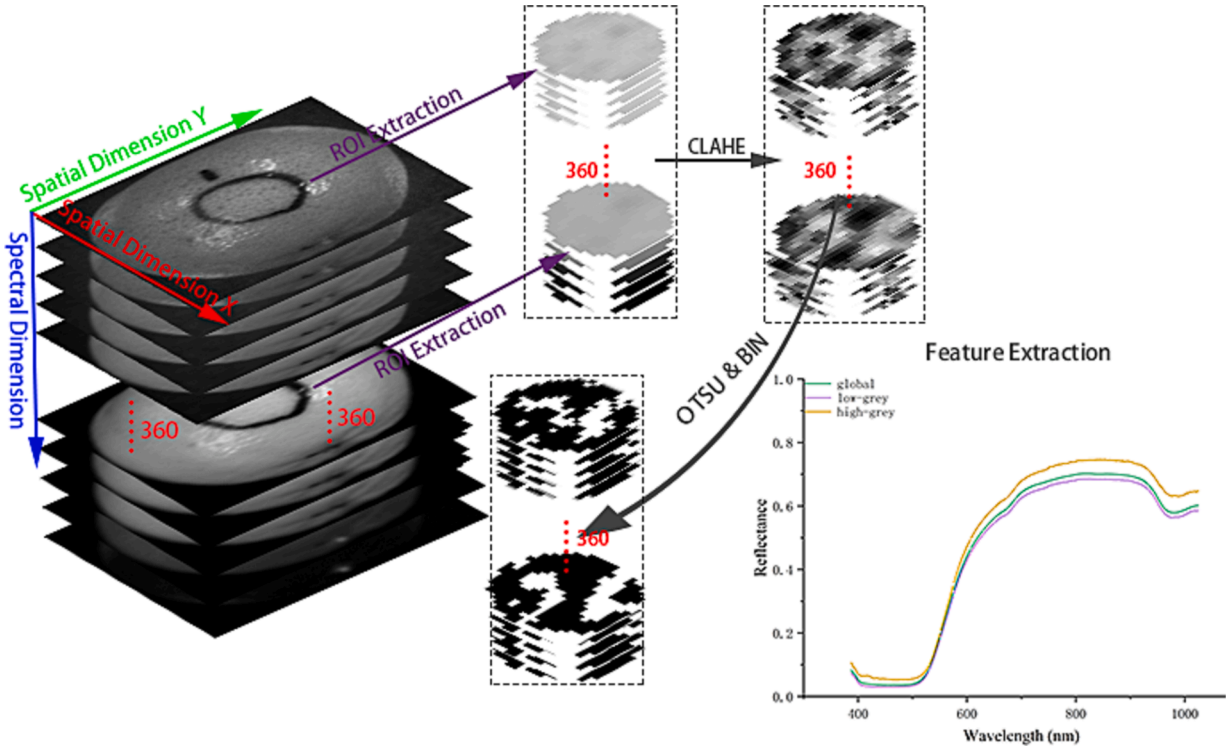

Fig. 5. Global and local spectral feature extraction.

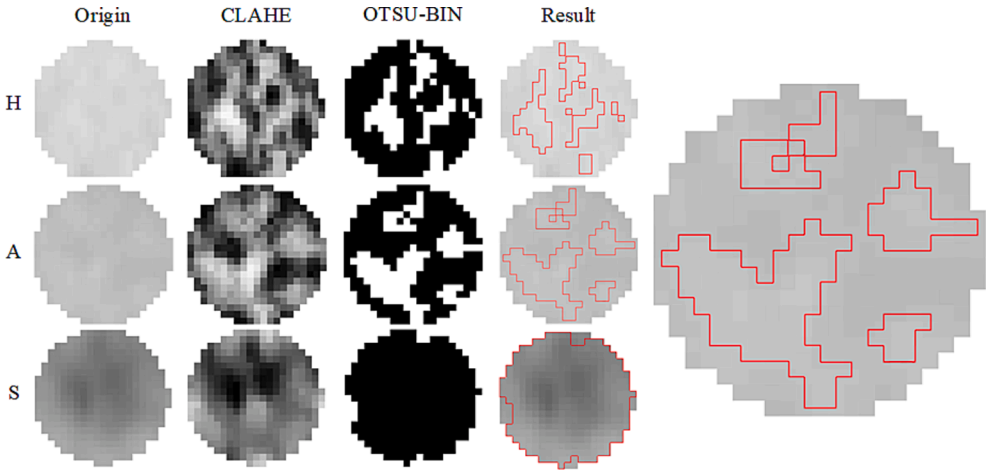

Fig. 6. Local area segmentation for different samples.

2.4. Classification model construction and validation

To evaluate the performance of different spectral features for the early detection of diseases, the support vector machine (SVM) (Bonah et al., 2020;Lu et al., 2020), k-nearest neighbour (k-NN) (Zhang & Ji, 2019;Pan et al., 2019) and RF (Siedliska et al., 2018;Che et al., 2018) were used as validation models. SVM is very effective for spectral data with a relatively small amount of data and high dimensions (Jiang et al., 2022;Huang et al., 2022). The SVM model selects the path that passes through the largest possible gap between different types of sample points as the hyperplane to obtain the best classification effect, and new sample points are classified into a certain class according to a certain face of the hyperplane where they fall. The k-NN algorithm usually uses three distance measures including the Manhattan distance, Euclidean distance and P-norm distance. Based on the selected distance measure, the K samples closest to the points to be classified are searched in the training dataset, and a class label is assigned to the new data points through the majority vote of the k-NN model (Pan et al., 2019). RF is an algorithm that integrates multiple trees through the idea of integrated learning. Its basic unit is the decision tree; when forecasting, each growing tree predicts its target class in a similar way to a decision tree, and the class that is voted on by the tree the most will become the class suggested by the classifier (Saha & Manickavasagan, 2021).

The hyperparameters of the classification models used in this study were adjusted using a grid search technique, and the average accuracy of the 10-fold-cross-validation of all data in the training and validation sets was used as the evaluation index to obtain the optimal hyperparameters of the model for different spectral features. Based on the hyper-parameters for different spectral features, the model was trained using the training set and the test set data were used to evaluate the classifi-cation performance of the model.

Three performance metrics, including the overall accuracy (A), recall rate (R), precision (P) and F1-score, were used to evaluate the performance of the classification model as defined in Eqs. (2)–(5).

$$A = \frac{TP + TN}{TP + FP + TN + FN} \tag{2}$$

$$R = \frac{TP}{TP + FN} \tag{3}$$

$$P = \frac{TP}{TP + FP} \tag{4}$$

$$\text{F1-score} = 2 \times \frac{P \times R}{P + R} \tag{5}$$

where TP indicates the number of samples belonging to the class that were correctly classified into this class, FN indicates the number of samples not belonging to the class that were incorrectly classified into this class, TN indicates the number of samples belonging to the class that were incorrectly classified into other classes of this class, and FP indicates the number of samples not belonging to the class that were correctly classified into other classes of this class.

3. Results and discussion

3.1. Spectral response curve analysis

To investigate the pattern of anthracnose development over time, the average spectral curves of all samples using GSFs were calculated for healthy and infected citrus fruit within 2–8 d after infection, as shown in Fig. 7. It can be noted that healthy samples had higher spectral reflectance values in the 550–950 nm spectral range, while symptomatic samples showed a gradual decrease in spectral reflectance with the increase of infection days. The decrease in spectral reflectance of symptomatic samples may be because the infestation of *C. gloeosporioides* disrupts the cellular structure of the epidermis, leading to the loss of compounds (e.g., carotenoids and soluble solids) in the sampled region, thus exhibiting lower reflectance in the spectral profile, and related studies have shown the existence of bands in the spectra that are sensitive to the functional groups of compounds. For example, Xie et al. reported that the spectral band near 750 nm is attributed to the third overtone of O–H and the fourth overtone of C–H, which reflect the content of compounds such as soluble solids in citrus (Xie & Lee, 2021). The statistical plot of anthracnose development shown in Fig. 4 also explains the pattern of spectral curves, where only a small number of citrus changed from asymptomatic to symptomatic within 4 d of successful inoculation with the causative fungus, and the overall trend of spectral curves of healthy and fungus-inoculated citrus was similar, but the reflectance of asymptomatic samples in the early stage of disease was slightly lower than that of healthy samples due to the reduction in the content of epidermal-related components. Over time, from day 5 onwards, the number of symptomatic samples increased, and the symptomatic citrus became progressively more severe, with the deepening of the black spots causing more light to be absorbed by the sampled area, which in turn led to a significant decrease in the overall spectral curve reflectance. In addition, there are some sensitive bands related to specific internal chemical compositions; for example, the band near 970 nm is related to the water absorption(Clevers et al., 2008), and that near 680 nm is related to chlorophyll *a* in the pericarp (Zhang et al., 2020) Thus, distinct spectral absorption valleys can be observed near these two bands, and the relevant components exhibit a decrease due to the development of anthracnose, which in turn causes the absorption valleys to plateau.

To investigate the distribution pattern of the spectral curves of samples with different infection degrees, the spectral curves of different samples using GSFs were extracted, and the average spectral curves of different samples were calculated, as shown in Fig. 8. The range of reflectance variation of healthy, asymptomatic and symptomatic samples increased sequentially, showing a gradual increase in interclass variance in the spectra of the three categories of samples. The spectral variability of healthy samples was mainly caused by the difference in epidermal composition of different individual citrus fruit, while the spectral variability of asymptomatic and symptomatic samples was caused by the different severities of lesions after the fungal infestation of the fruit. Moreover, there are a small number of similar spectral profiles between asymptomatic samples and the other two types of samples, and these similar spectra are distributed in the early and late asymptomatic stages, with similar spectral responses to healthy and symptomatic early samples, respectively. The samples with similar spectra can pose a great challenge for early detection, and the approximate overlap of the spectral curve distribution of such samples also suggests that it is not sufficient to accurately distinguish the different samples based on a single sensitive wavelength alone and that better classification may be obtained when more bands are analyzed (Gao et al., 2020).

To explore the differences between the global and local spectral features, the average spectral curves of different samples under different spectral features are given as shown in Fig. 9. The average spectral curves of different samples show differences in the average spectral reflectance magnitude in different spectral features. The amplitudes of the GSFs of the three categories of samples under different bands are between the HSFs and LSFs, where the GSFs have a lower difference in magnitude from the LSFs than from the HSFs, while there is a more obvious magnitude shift from the HSFs, which may be the reason why the HSFs represent the high-brightness region of the band image, as shown in Fig. 6. After the local area segmentation process, the low greyscale regions occupy most of the pixels of the entire ROI, and the resulting extracted mean spectrum has a lower difference in magnitude from the GSFs, while the high greyscale regions consist of only a small number of pixels and have a higher difference in magnitude from the GSFs, which indicates that the combination of HSFs and GSFs with greater spectral signature differences may be more favourable for pattern classification. Moreover, it can be noted that the interclass variance of different samples is smaller in the GSFs and LSFs at the 400–530 nm band, while the HSFs provide a larger interclass variance, which also indicates that the HSFs may be more favourable for the classification of three patterns.

3.2. Early detection of citrus anthracnose based on fused spectral features

3.2.1. Classification based on the full spectra

To investigate the effects of global and local spectral features on the early detection of citrus anthracnose, SVM, k-NN and RF models were used to classify healthy, asymptomatic and symptomatic samples, and their 10-fold-cross-validation results using training and validation sets are shown in Table 1, where the average classification accuracy for the three types of samples are given. Furthermore, for all the following experiments, the optimal setting of the number (the parameter k) of nearest neighbours involved in the k-NN algorithm was carried out using a 10-fold cross-validation procedure and the training dataset.

As shown in Table 1, the classification performance of the SVM and RF models is better than that of the k-NN model for different spectral features, The possible reason is that the k-NN model directly makes the determination of category attribution by finding the k training samples closest to the test sample points in the hypothesis space, while in early disease detection, the existence of similar spectra between different categories of samples mentioned in Section 3.1, which are similarly distributed in the hypothesis space of the k-NN model, leads to the lower classification accuracy obtained by the k-NN model. In contrast, the SVM and RF models change the distribution of samples in the hypothesis space by means of kernel function mapping and pruning of each tree feature, respectively, which has the probability of making the samples obtain a greater separation from each other, which will help reduce the difficulty of classification. From the classification results of the SVM and RF models, we can see that the classification performance of the model is further improved by fusing global and local spectral features compared with the traditional GSFs-based approach, and the more significant classification performance improvement is with the increase in local spectral features. Although the two classifiers show similar classification performance for different spectral features, the classification performance improvement of the SVM model is more significant, which is consistent with the better classification results achieved by the SVM model when using the SVM and RF models for the early detection of mango anthracnose, as reported by Ardila et al. (2020). The reason for this phenomenon may be that the application of the kernel function of the SVM model allows it to handle high-dimensional data relatively well.

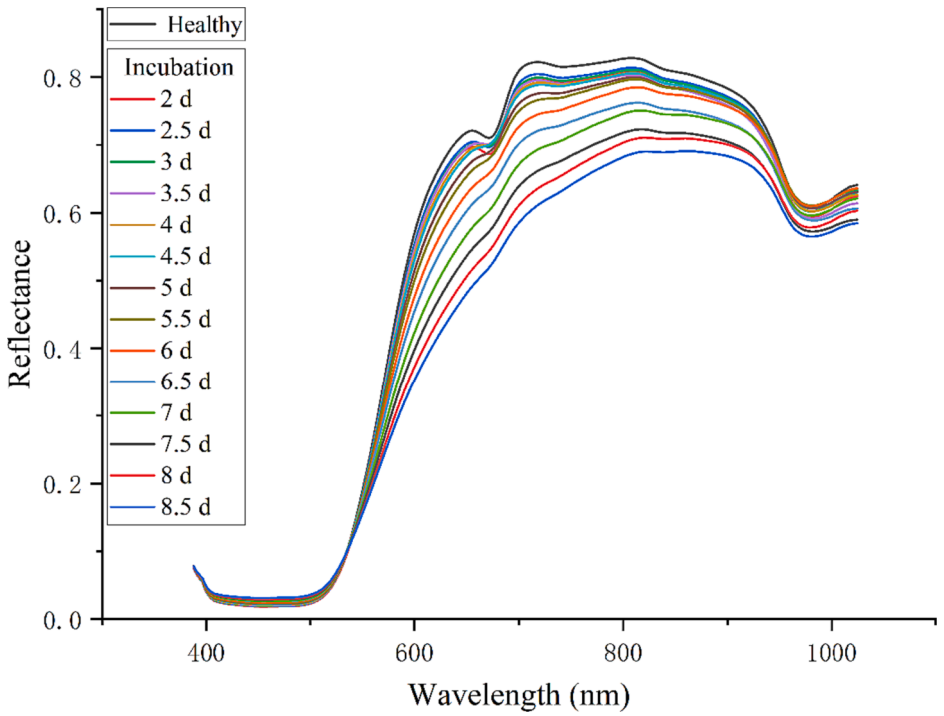

Fig. 7. Average spectral curves of healthy and different infection time samples.

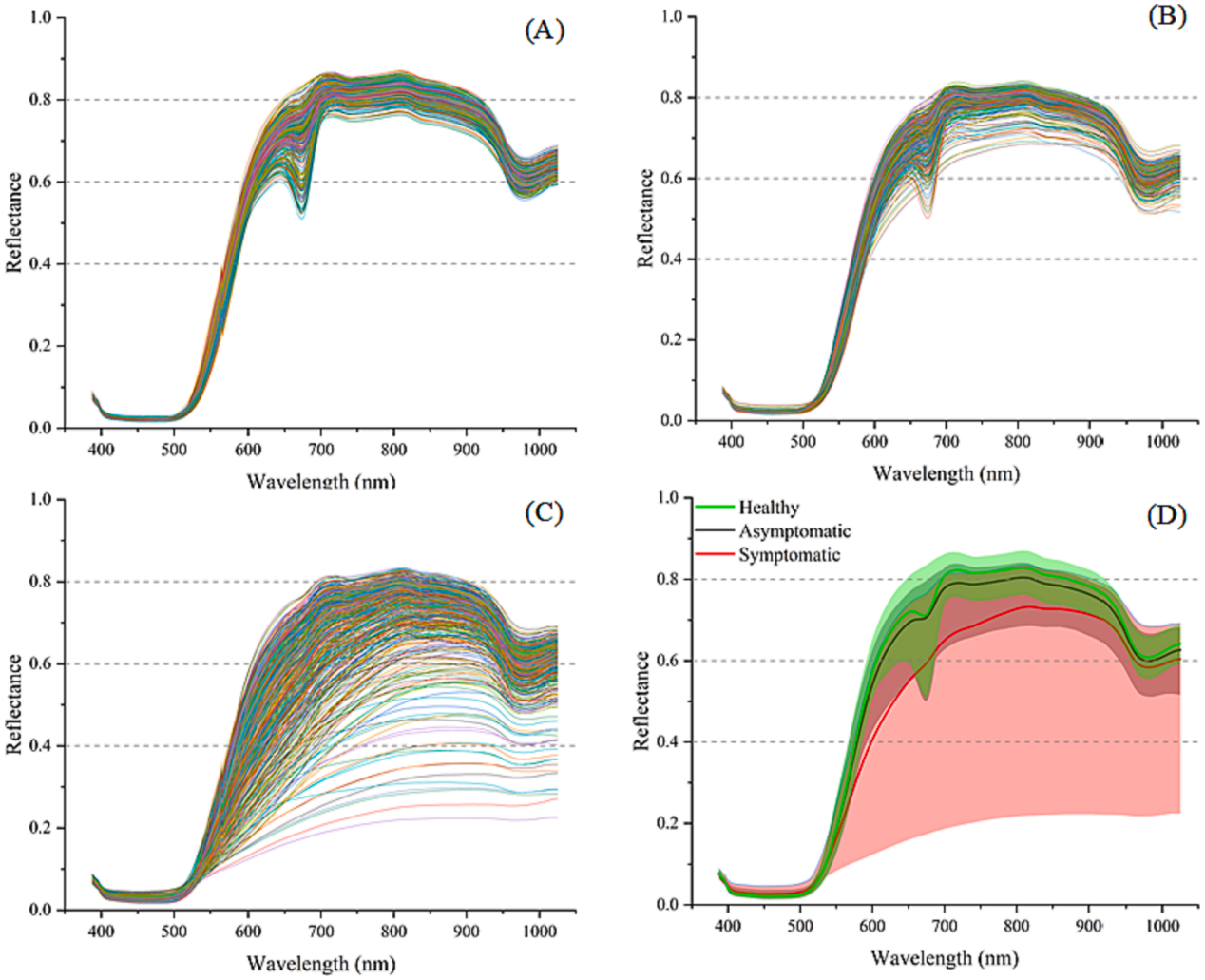

Fig. 8. Spectral curves of samples with different infection degrees: (A) healthy, (B) asymptomatic, (C) symptomatic, (D) spectral curve distribution of the three types of samples.

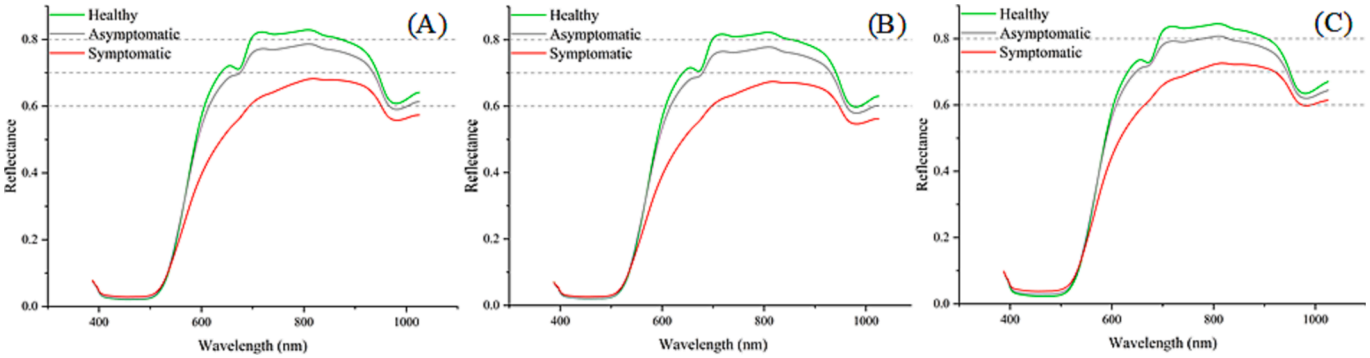

Fig. 9. Average spectral curves of the three types of samples with different spectral features: (A) GSFs, (B) LSFs, (C) HSFs.

Table 1
Cross validation results using different spectral features for the SVM, k-NN and RF models based on full spectra.

Spectral features	Model		
	SVM	k-NN	RF
GSFs	0.8989 ± 0.0274	0.8796 ± 0.0318	0.8952 ± 0.0262
GSFs + LSFs	0.9086 ± 0.0296	0.8819 ± 0.0207	0.8991 ± 0.0274
GSFs + HSFs	0.9093 ± 0.0166	0.8859 ± 0.0293	0.9011 ± 0.0253
GSFs + LSFs + HSFs	**0.9197 ± 0.0211**	0.9019 ± 0.0292	0.9026 ± 0.0263

As shown in Table 1, all three different models showed similar classification patterns for different spectral features, with the overall classification accuracy of the models improving as the number of features increased. When using GSFs, the SVM model has produced the best classification results, where the average classification accuracy is 89.89 %. When the local spectral features are added to the GSFs, the classification performance of the model using HSFs is better than that using LSFs. The average classification accuracy of GSFs + HSFs in the SVM model is 90.93 %, which is consistent with the assumption that HSFs are more beneficial to the classification of three patterns given in Section 3.1. When the GSFs are applied with both the LSFs and HSFs at the same time, it can reflect the spectral features of the global area and local details of the sampling area. Different local spectral features explain the differences in the local areas of different samples in different band images, which makes the learning model show better classification performance in a higher-dimensional hypothetical space, with an average classification accuracy of 91.97 %, which can more effectively classify the three images of samples.

To further evaluate the influence of the fused spectral features on pattern classification, based on the test data. Moreover, to evaluate the run-time complexity of the combination of different feature extraction procedures and machine learning models, the average elapsed time of 10 independent runs of each combination was calculated. Table 2 shows the classification performance for the SVM, k-NN and RF models using different spectral features and Fig. 10 shows the classification results in the SVM model using GSFs and GSFs + LSFs + HSFs. For the three classification models, the F1-score for each class of samples can reflect the performance of early detection. As shown in Table 2, when GSFs + LSFs + HSFs were used, the F1-score for three classes of samples significantly outperformed the conventional GSFs-based method. The overall F1-score for the three classes of samples performed best in the SVM model, managing to reach 95.35 %, 87.25 % and 93.40 % respectively. As shown in Fig. 10, when using the SVM model, it can be seen that healthy and symptomatic samples can be accurately distinguished by different spectral features. For both healthy and asymptomatic samples, many samples would be misclassified if only traditional GSFs were used. However, when GSFs are fused with local spectral features, the misclassification is greatly improved and the model has much higher recall and accuracy for both healthy and asymptomatic classes. The relatively high error correlation between the two patterns for asymptomatic and symptomatic samples may be attributed to the presence of samples with similar spectra. Samples distributed between late asymptomatic and early symptomatic had no obvious symptoms or mild early symptoms, but their spectral features did not differ significantly in most bands, which leads to the inaccurate classification of trained models. As indicated in Table 2, the runtime complexity of the presented spectral feature extraction procedure, i.e., the spectral features termed by “GSFs + LSFs + HSFs”, could still guarantee similar calculation complexity compared to the conventional spectral features. In brief, the experimental results demonstrate that the fusion of global and local spectral features could provide complementary information between different feature representations. Specifically, compared to the feature representation using only the conventional GSFs, the addition of local spectral feature, i.e., LSFs and HSFs, aided to compensate for the spectral distribution of different local image channels, and thus more accurate detection result of citrus anthracnose was obtained.

Table 2
Classification performance for the SVM, k-NN and RF models using different spectral features.

Model	Spectral features	Accuracy		Precision	Recall rate	F1-score	Time (s)
SVM	**GSFs**	0.8902	**H**	0.8955	0.9449	0.9195	1.2185
			A	0.8602	0.7692	0.8122	
			S	0.9091	0.9434	0.9259	
	GSFs + LSFs + HSFs	**0.9228**	**H**	0.9389	0.9685	**0.9535**	1.6402
			A	0.8900	0.8558	**0.8725**	
			S	0.9340	0.9340	**0.9340**	
k-NN	**GSFs**	0.8724	**H**	0.8797	0.9213	0.9000	0.1094
			A	0.8081	0.7692	0.7882	
			S	0.9238	0.9151	0.9194	
	GSFs + LSFs + HSFs	**0.9021**	**H**	0.8750	0.9921	**0.9299**	0.3334
			A	0.8989	0.7692	**0.8290**	
			S	0.9423	0.9245	**0.9333**	
RF	**GSFs**	0.8932	**H**	0.9044	0.9685	0.9354	0.578
			A	0.8586	0.8173	0.8374	
			S	0.9118	0.8774	0.8942	
	GSFs + LSFs + HSFs	**0.9139**	**H**	0.9370	0.9370	**0.9370**	0.9685
			A	0.8440	0.8846	**0.8638**	
			S	0.9604	0.9151	**0.9372**	

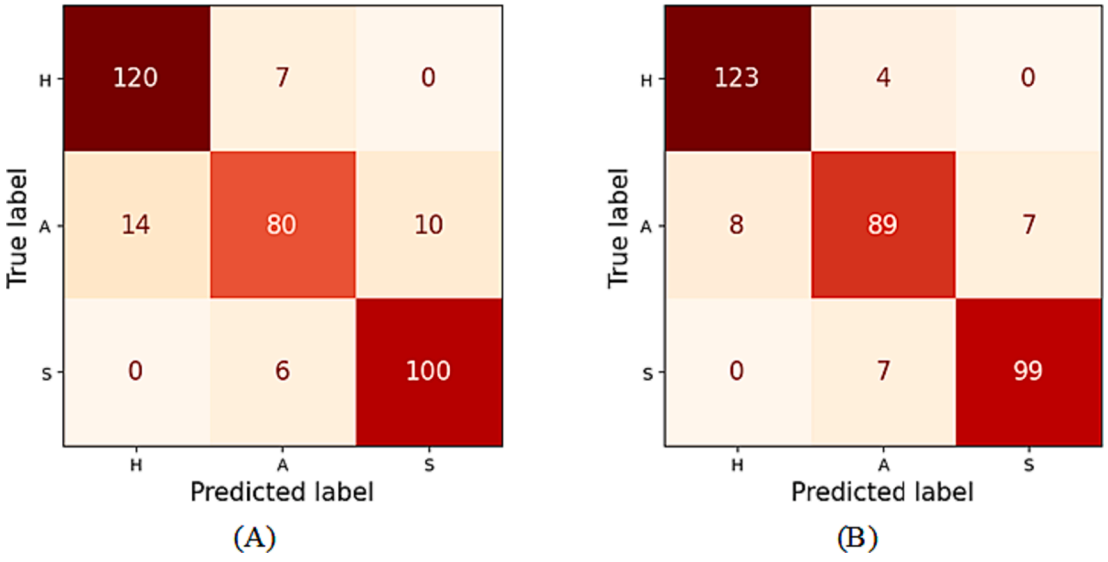

Fig. 10. Confusion matrix of SVM classification results using different spectral features: (A) GSFs, (B) GSFs + LSFs + HSFs.

3.2.2. Classification based on spectra of selected optimal wavelengths

SPA as a forward variable selection method has been widely used in optimal wavelengths selection (Chen et al., 2022;Gao & Xu, 2022;Xu et al., 2022). In this study, the SPA procedure was used to process a matrix of GSFs based on full spectra composed of all samples, and as shown in Fig. 11, a minimum number of 15 wavelengths were obtained without significantly reducing the RMSE, which were located at 456, 517, 531, 542, 552, 576, 608, 631, 652, 675, 690, 728, 909, 934, and 971 nm. These sets of wavelengths with minimal collinearity were subsequently used to extract HSFs and LSFs at the corresponding wavelengths, and the fused spectral features of different samples at the optimal wavelengths were formed by concatenating the feature layers. In the analysis based on full spectra, superior classification perfor-mance was obtained by fusing global and local spectral features than the conventional GSFs-based method. The classification performance of the three models was subsequently evaluated based on different spectral features at optimal wavelengths, and the cross-validation results are shown in Table 3. As can be seen from the table, using GSFs + LSFs + HSFs, the SVM and RF models still manage to show better classification performance than the k-NN model. In the SVM model using GSFs + LSFs + HSFs, the average classification accuracy was 91.04 %, an improvement of 3.01 % compared to the conventional GSFs-based method. The reduction in spectral wavelengths leads to a reduction in sample features, which often affects the classification performance of the model. For example, when using GSFs and GSFs + LSFs + HSFs based on the optimal wavelengths, the classification performance of the SVM model is inferior to that based on the full spectra, but it is worth noting that when using GSFs + LSFs + HSFs at optimal wavelengths, GSFs at optimal wavelengths are obtained, which also complemented the local information of LSFs and HSFs under these bands and obtained superior classification performance in the SVM model than using conventional GSFs, whether based on the full spectra or the spectra of optimal wavelengths. This demonstrates that the method achieves a high classification accuracy while reducing the number of wavelengths, which is substantial for practical industrial applications.

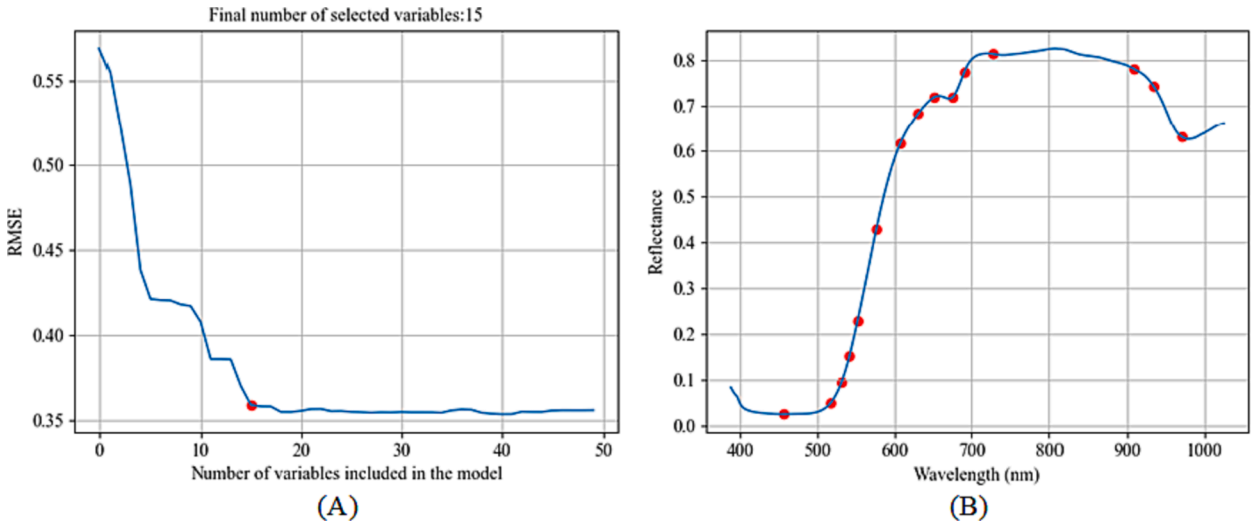

Fig. 11. Optimal wavelength selection using SPA: (A) number of optimal candidate variables base on RMSE of the MLR, (B) distribution of optimal wavelengths.

Table 3
Cross validation results using different spectral features in three models based on optimal wavelengths.

Spectral features	Model		
	SVM	k-NN	RF
GSFs	0.8803 ± 0.0294	0.8892 ± 0.0301	0.8926 ± 0.0324
GSFs + LSFs	0.8967 ± 0.0315	0.8945 ± 0.0296	0.9004 ± 0.0222
GSFs + HSFs	0.8981 ± 0.0257	0.9071 ± 0.0271	0.9019 ± 0.0249
GSFs + LSFs + HSFs	**0.9104 ± 0.0165**	0.9041 ± 0.0257	0.9063 ± 0.0267

4. Conclusion

In this study, an effective and efficient method for early detection of citrus anthracnose using HSI and machine learning techniques was proposed. The proposed spectral feature extraction procedure aims to extract the different local spectra from the bright and dark regions of the ROI within each band image, which provides some complementary information for the conventional mean spectrum of the global ROI. The fused spectral features obtained by concatenating the local spectral features and the conventional global spectral features of the ROI could obtain better results for the early detection of citrus anthracnose. Compared with the k-NN and RF classifiers, the extracted full fused spectral features combined with the SVM classifier performed better in the early detection of citrus anthracnose, where the resultant average detection accuracy reached 91.97%. Moreover, the dimensionally-reduced fused spectral features by SPA also obtained acceptable detection results while combining the SVM classifier, where the average detection accuracy was 91.04%.

Acknowledgements

The authors acknowledge support from the Planned Science and Technology Project of Guangdong Province, China (Grant Nos. 2019B020216001, 2019A050510045, and 2021A0505030075), the National Natural Science Foundation of China (Grant No. 32071895), the Natural Science Foundation of Guangdong Province, China (Grant Nos. 2020B1515120070, 2021A1515010824 and 2022A1515010885), the Key Project of Universities in Guangdong Province, China (Grant No. 2020ZDZX1061), the Innovation Team Project of Universities in Y. Tang et al. Guangdong Province, China (Grant No. 2021KCXTD010), the Planned Science and Technology Project of Guangzhou, China (Grant Nos. 202002020063, 202007040007, and 202103000028), and the Rural Revitalization Strategy Project of Guangdong Province, China (Grant No. 2019KJ138).

References

Ardila, C.E.C., Ramirez, L.A., Ortiz, F.A.P., 2020. Spectral analysis for the early detection of anthracnose in fruits of Sugar Mango (Mangifera indica). Comput. Electron. Agr. 173, 105357 https://doi.org/10.1016/j.compag.2020.105357.

Babellahi, F., Paliwal, J., Erkinbaev, C., Amodio, M.L., Chaudhry, M.M.A., Colelli, G., 2020. Early detection of chilling injury in green bell peppers by hyperspectral imaging and chemometrics. Postharvest Biol. Tec. 162, 111100 https://doi.org/10.1016/j.postharvbio.2019.111100.

Bonah, E., Huang, X., Yi, R., Aheto, J.H., Yu, S., 2020. Vis-NIR hyperspectral imaging for the classification of bacterial foodborne pathogens based on pixel-wise analysis and a novel CARS-PSO-SVM model. Infrared Phys. Techn. 105, p. 103220-. https://doi.org/10.1016/j.infrared.2020.103220.

Castorena, J., Morrison, J., Paliwal, J., Erkinbaev, C., 2015. Non-uniform system response detection for hyperspectral imaging systems. Infrared Phys. Techn. 73, 263–268. https://doi.org/10.1016/j.infrared.2015.10.002.

Che, W., Sun, L., Zhang, Q., Tan, W., Ye, D., Zhang, D., Liu, Y., 2018. Pixel based bruise region extraction of apple using Vis-NIR hyperspectral imaging. Comput. Electron. Agr. 146, 12–21. https://doi.org/10.1016/j.compag.2018.01.013.

Chen, J., Bai, T., Zhang, N., Zhu, L., Zhang, X., 2022. Hyperspectral detection of sugar content for sugar-sweetened apples based on sample grouping and SPA feature selecting methods. Infrared Phys. Techn., 104240 https://doi.org/10.1016/j.infrared.2022.104240.

Clevers, J.G., Kooistra, L., Schaepman, M.E., 2008. Using spectral information from the NIR water absorption features for the retrieval of canopy water content. Int. J. Appl. Earth Obs. 10 (3), 388–397. https://doi.org/10.1016/j.jag.2008.03.003.

Gao, Z., Khot, L.R., Naidu, R.A., Zhang, Q., 2020. Early detection of grapevine leafroll disease in a red-berried wine grape cultivar using hyperspectral imaging. Comput. Electron. Agr. 179, 105807 https://doi.org/10.1016/j.compag.2020.105807.

Gao, S., Xu, J., 2022. Hyperspectral image information fusion-based detection of soluble solids content in red globe grapes. Comput. Electron. Agri. 196, 106822 https://doi.org/10.1016/j.compag.2022.106822.

Gui, J., Fei, J., Wu, Z., Fu, X., Diakite, A., 2021. Grading method of soybean mosaic disease based on hyperspectral imaging technology. Informat. Process. Agri. 8 (3), 380–385. https://doi.org/10.1016/j.inpa.2020.10.006.

Huang, X., Meng, Q., Wu, Z., He, F., Tian, P., Lin, J., Zhu, H., Zhou, X., Huang, Y., 2022. Detection of early bruises in Gongcheng persimmon using hyperspectral imaging. Infrared Phys. Techn. 125, 104316 https://doi.org/10.1016/j.infrared.2022.104316.

Jiang, H., Zhang, C., He, Y., Chen, X., Liu, F., Liu, Y., 2016. Wavelength selection for detection of slight bruises on pears based on hyperspectral imaging. Appl. Sci. 6 (12), 450. https://doi.org/10.3390/app6120450.

Jiang, H., Liu, L., Chen, Q., 2022. Rapid determination of acidity index of peanuts by near-infrared spectroscopy technology: Comparing the performance of different near-infrared spectral models. Infrared Phys. Techn. 125, 104308 https://doi.org/10.1016/j.infrared.2022.104308.

Jiang, X., Zhen, J., Miao, J., Zhao, D., Wang, J., Jia, S., 2021. Assessing mangrove leaf traits under different pest and disease severity with hyperspectral imaging spectroscopy. Ecol. Ind. 129, 107901 https://doi.org/10.1016/j.ecolind.2021.107901.

Liu, D., Sun, D., Zeng, X., 2014. Recent advances in wavelength selection techniques for hyperspectral image processing in the food industry. Food Bioprocess Tech. 7 (2), 307–323. https://doi.org/10.1007/s11947-013-1193-6.

Lu, B., Jun, S., Ning, Y., Xiaohong, W., Xin, Z., 2021. Identification of tea white star disease and anthrax based on hyperspectral image information. J. Food Process Eng 44 (1), e13584.

Lu, Y., Wang, W., Huang, M., Ni, X., Chu, X., Li, C., 2020. Evaluation and classification of five cereal fungi on culture medium using Visible/Near-Infrared (Vis/NIR) hyperspectral imaging. Infrared Phys. Techn. 105, 103206 https://doi.org/10.1016/j.infrared.2020.103206.

Ma, P., Ren, J.C., Sun, G.Y., Zhao, H.M., Jia, X.P., Yan, Y.J., Zabalza, J., 2023. Multiscale superpixelwise prophet model for noise-robust feature extraction in hyperspectral images. IEEE Trans. Geosci. Remote. Sens. 61, 5508912. https://doi.org/10.1109/TGRS.2023.3260634.

Martinelli, F., Scalenghe, R., Davino, S., Panno, S., Scuderi, G., Ruisi, P., Villa, P., Stroppiana, D., Boschetti, M., Goulart, L.R., 2015. Advanced methods of plant disease detection. A Review. Agron. Sustain. Dev. 35 (1), 1–25. https://doi.org/10.1007/s13593-014-0246-1.

Nadimi, M., Brown, J.M., Morrison, J., Paliwal, J., 2021. Examination of wheat kernels for the presence of Fusarium damage and mycotoxins using near-infrared hyperspectral imaging. Measurement: Food 4, 100011. https://doi.org/10.1016/j.meafoo.2021.100011.

Pan, T., Chyngyz, E., Sun, D., Paliwal, J., Pu, H., 2019. Pathogenetic process monitoring and early detection of pear black spot disease caused by Alternaria alternata using hyperspectral imaging. Postharvest Biol. Tec. 154, 96–104. https://doi.org/10.1016/j.postharvbio.2019.04.005.

Ruiz-Ruiz, S., Ambrós, S., Del Carmen Vives, M., Navarro, L., Moreno, P., Guerri, J., 2009. Detection and quantitation of Citrus leaf blotch virus by TaqMan real-time RT-PCR. J. Virol. Methods 160 (1–2), 57–62. https://doi.org/10.1016/j.jviromet.2009.04.012.

Saccon, F.A., Parcey, D., Paliwal, J., Sherif, S.S., 2017. Assessment of Fusarium and deoxynivalenol using optical methods. Food Bioprocess Tech. 10 (1), 34–50. https://doi.org/10.1007/s11947-016-1788-9.

Saha, D., Manickavasagan, A., 2021. Machine learning techniques for analysis of hyperspectral images to determine quality of food products: A review. Curr. Res. Food Sci. 4, 28–44. https://doi.org/10.1016/j.crfs.2021.01.002.

Sajadi, S., Fathi, A., 2020. Genetic algorithm based local and global spectral features extraction for ear recognition. Expert Syst. Appl. 159 https://doi.org/10.1016/j.eswa.2020.113639.

Siedliska, A., Baranowski, P., Zubik, M., Mazurek, W., Sosnowska, B., 2018. Detection of fungal infections in strawberry fruit by VNIR/SWIR hyperspectral imaging. Postharvest Biol. Tec. 139, 115–126. https://doi.org/10.1016/j.postharvbio.2018.01.018.

Singh, V., Sharma, N., Singh, S., 2020. A review of imaging techniques for plant disease detection. Artificial Intelligence in Agriculture 4, 229–242. https://doi.org/10.1016/j.aiia.2020.10.002.

Tian, Y., Zhao, Y., Chen, B., Shuo, C., Rong, Z., Hu, B., Xiang, L., 2020. Real-time PCR assay for detection of Dickeya fangzhongdai causing bleeding canker of pear disease in China. J. Integr. Agr. 19 (4), 898–905. https://doi.org/10.1016/S2095-3119(19)62881-9.

Weng, H., Lv, J., Cen, H., He, M., Zeng, Y., Hua, S., Li, H., Meng, Y., Fang, H., He, Y., 2018. Hyperspectral reflectance imaging combined with carbohydrate metabolism analysis for diagnosis of citrus Huanglongbing in different seasons and cultivars. Sens. Actuators B 275, 50–60. https://doi.org/10.1016/j.snb.2018.08.020.

Xie, C., Lee, W.S., 2021. Detection of citrus black spot symptoms using spectral reflectance. Postharvest Biol. Tec. 180, 111627 https://doi.org/10.1016/j.postharvbio.2021.111627.

Xu, S., Ren, J., Lu, H., Wang, X., Sun, X., Liang, X., 2022. Nondestructive detection and grading of flesh translucency in pineapples with visible and near-infrared spectroscopy. Postharvest Biol. Tec. 192, 112029 https://doi.org/10.1016/j.postharvbio.2022.112029.

Xuan, G., Li, Q., Shao, Y., Shi, Y., 2022. Early diagnosis and pathogenesis monitoring of wheat powdery mildew caused by blumeria graminis using hyperspectral imaging. Comput. Electron. Agr. 197, 106921 https://doi.org/10.1016/j.compag.2022.106921.

Yeh, Y., Chung, W., Liao, J., Chung, C., Kuo, Y., Lin, T., 2016. Strawberry foliar anthracnose assessment by hyperspectral imaging. Comput. Electron. Agr. 122, 1–9. https://doi.org/10.1016/j.compag.2016.01.012.

Zhang, L., Ji, H., 2019. Identification of wheat grain in different states based on hyperspectral imaging technology. Spectrosc. Lett. 52 (6), 1–11. https://doi.org/10.1080/00387010.2019.1639762.

Zhang, J., Timmer, L.W., 2007. Preharvest application of fungicides for postharvest disease control on early season tangerine hybrids in Florida. Crop Prot. 26 (7), 886–893. https://doi.org/10.1016/j.cropro.2006.08.007.

Zhang, H., Zhang, S., Dong, W., Luo, W., Huang, Y., Zhan, B., Liu, X., 2020. Detection of common defects on mandarins by using visible and near infrared hyperspectral imaging. Infrared Phys. Techn. 108, 103341 https://doi.org/10.1016/j.infrared.2020.103341.

Li Y.H., Ren J.C., Yan Y.J. Liu Q.Y., Ma P., Petrovski A., Sun H.J., 2023. CBANet: an end-to-end cross-band 2-D attention network for hyperspectral change detection in remote sensing. IEEE Trans. Geosci. Remote. Sens. 61, 5513011. doi: 10.1109/TGRS.2023.3276589.